nature communications

Article

https://doi.org/10.1038/s41467-025-56436-2

A tunable entangled photon-pair source based on a Van der Waals insulator

Received: 28 August 2024

Accepted: 20 January 2025

Published online: 23 February 2025

Check for updates

Xiaodan Lyu[1], Leevi Kallioniemi[1], Hao Hong[2], Rui Qu[3], Yan Zhang[1], Jesus Zúñiga-Perez[1,4], Kaihui Liu[2] ✉ & Weibo Gao[1,3,5] ✉

Scalable quantum photonic devices drive the development of compact sources of entangled photons, which are pivotal for quantum communication, computing, and cryptography. In this work, we present entangled photon pair generation in rhombohedral boron nitride (r-BN), leveraging its unique optical and structural properties. Unlike conventional hexagonal boron nitride, which suffers from reduced nonlinear response due to centrosymmetric structure in even-layered stacks, r-BN features interlayer ABC stacking and maintains robust in-plane inversion symmetry. These characteristics lead to highly efficient entangled photon generation. Our system demonstrates an entangled photon pair generation rate up to 8667 Hz/(mW·mm) and offers a tunable platform for Bell state generation by simply adjusting the pump polarization, without compromising the entanglement quality or generation efficiency. The polarization entangled state is measured with a fidelity up to 94%. This advancement not only marks a significant step towards ultrathin, scalable quantum devices but also establishes r-BN as a promising candidate for on-chip integrated quantum optical applications.

Entangled photon pairs are critical resources to the advancement of quantum technologies, enabling groundbreaking applications in quantum communications[1], quantum metrology[2,3], and quantum imaging[4–6]. Traditionally, spontaneous parametric down-conversion (SPDC)[7–9], an efficient way for generation of entangled photon pairs, has relied on bulk nonlinear optical materials like lithium niobate[10,11] and beta barium borate[9]. Over the past decade, significant research has focused on flat-optics platforms, including microstructures on lithium niobate, which leverage long propagation lengths in waveguides, as well as other structures like micro-ring resonators[12,13]. Nonlinear flat-optics devices offer several advantages, including their slim profile, ultrafast and broadband operation, and relaxed phase-matching requirements for frequency conversion[14–17]. Polarization entanglement has been demonstrated in qubit and qutrit systems using nonlinear thin films, such as gallium phosphide films[16], liquid crystals[17] and epsilon-near-zero metasurface platforms[18].

Recently, van der Waals materials have gained attention due to their interlayer van der Waals forces that allow for easy stacking and integration[19] without the need for lattice matching typically required in conventional materials. This feature, along with their relaxed phase-matching conditions[20], makes them highly suitable candidates for integration into nanoscale quantum devices. Despite their promising qualities, several challenges persist in utilizing them as photon pair emitters. First, low scalability and brightness, as the absolute signal yield in monolayer nonlinear conversion is very low due to the short interaction length with the medium[21]. For materials such as 2H-phase transition-metal dichalcogenides, despite their high second-order nonlinear susceptibilities in monolayers, upon layering, AB stacking order between layers severely quench the nonlinear response, limiting their scalability for high-performance quantum optical applications[22,23]. Consequently, recent efforts have focused on inversion-symmetry-broken van der

[1]Division of Physics and Applied Physics, School of Physical and Mathematical Sciences, Nanyang Technological University, Singapore, Singapore. [2]School of Physics, Peking Univeristy, Beijing, China. [3]Centre for Quantum Technologies, National University of Singapore, Singapore, Singapore. [4]Majulab, International Research Laboratory IRL 3654, CNRS, Université Côte d'Azur, Sorbonne Université, National University of Singapore Nanyang Technological University, Singapore, Singapore. [5]School of Electrical and Electronic Engineering, Nanyang Technological University, Singapore, Singapore.
✉e-mail: khliu@pku.edu.cn; wbgao@ntu.edu.sg

Waals materials for generating polarization entanglement[24,25]. Second, 2D semiconductors suffer from generally high photoluminescence (PL) signal[26] that adds to the background noise at the nonlinear excitation, increasing the accidental counts, complicating the isolation of entangled pairs and reducing the clarity of quantum signals. This needs to be counteracted by spectral filtering and placement of the photon pair signal outside the spectral band of the PL signal, which on the other hand, limits the operation wavelength of quantum emitters[24,25]. Third, while some reported 2D materials with high nonlinearities have the potential to generate spectral or spatial entanglement, they do not inherently produce polarization-entangled states[20]. For instance, materials like $NbOCl_2$ require additional device architectures, such as cross-stacked layers or additional optical paths[27–29], to induce polarization entanglement, which can complicate device design and fabrication.

In this study, we leverage the properties of rhombohedral boron nitride (r-BN) to develop a class of entangled photon-pair sources that are not only more compact but also capable of higher performance compared to traditional materials. Unlike its hexagonal counterpart, r-BN exhibits broken out-of-plane inversion symmetry while preserving in-plane inversion symmetry[30–32], which increases the signal yield of nonlinear conversion, making it a robust nonlinear optical source. The unique crystal symmetry makes it possible to intrinsically emit polarization entangled states. The wide optical bandgap makes r-BN not to have strong photoluminescence as other 2D semiconductors[30]. The physicochemical stability and high laser damage threshold also makes it an ideal host for SPDC processes[31].

In this work, we demonstrate experimentally the generation of polarization-entangled photons from r-BN, showing the realization of quantum entanglement in a van der Waals insulator. The state of photon pairs can be controlled by rotating the pump field polarization and we verify that the created photon pairs exhibit quantum coherence. By aligning the polarization onto the zigzag or armchair direction, we successfully generate different Bell states. We observe a high entangled photon pair generation rate, good polarization visibility and a close resemblance with the expected state.

The generation of entangled photons using van der Waals insulators underscores their distinct benefits in quantum optics and sets the stage for further progress in integrated quantum photonics[33–35]. The broad spectral range inherent to these thin layers renders them ideal for exploring hyperentanglement across multiple frequency modes[15,36] (Supplementary Fig. 2). By leveraging van der Waals forces, these materials can be deposited over nanophotonic waveguides, further enhancing their nonlinear optical properties. The thermal stability and chemical inertness of these materials also enable direct nanostructuring on them[37]. Therefore, utilization of van der Waals insulators, such as r-BN, could bring substantial advancement in quantum information science, leading to more compact and efficient systems.

Results

Characterization of emitted photon pairs from r-BN flake

While monolayer BN exhibits a hexagonal structure belonging to space group D_{3h}, characterized by its centrosymmetry, multilayer r-BN breaks this symmetry with ABC stacking order in the out of plane direction. This inherent physical structure forms the basis for a notably nonlocal response, as the interaction between light and matter scales up with increasing number of layers, as illustrated in Fig. 1a. We used atomic force microscopy (AFM) to determine the thickness of our r-BN flake, which was measured to be 1.47 µm (Supplementary Fig. 1). We use a Hanbury Brown-Twiss setup[38] to characterize the photon pairs (Fig. 1b). The signal collection in our setup is based on back-reflection, which makes the whole setup more compact. As the excitation source, continuous-wave (CW) laser centered at 409 nm is reflected towards the sample with a dichroic mirror. The signal and idler photons from the sample pass through the same dichroic mirror, whose states can be projected to an arbitrary polarization state by a combination of quarter waveplate, half waveplate and polarizer before being coupled into a single mode fiber and collected by the photon detectors. The arrival times from photon detectors are resolved by a time tagger, which allows us to count the coincidences from the photon pair emission.

When the polarizations of both collection arms are aligned parallel to the excitation axis, the SPDC response measured on r-BN exhibits a distinctive coincidence peak at a zero-time difference between the two detector channels, indicating biphoton generation (Fig. 1c). As the pump power increases, the coincidence count rate rises linearly, consistent with expectations (Fig. 1d inset). Figure 1d presents the coincidence-to-accidental ratio (CAR) as a function of pump power, highlighting the non-classical nature of photon emission from r-BN. As depicted, CAR decreases as the pump power increases, reflecting the trade-off between increased photon generation rates and noise levels. With the current setup, a CAR value exceeding 100 was achieved at a pump power of 0.25 mW. Further optimization, including the use of a narrower 44 nm bandpass filter and a smaller time bin width of 0.5 ns, led to a CAR exceeding 1000 at a pump power of 2.5 mW (Supplementary Fig. 4). When using a 12 nm bandpass filter, the CAR reached approximately 2700 (Fig. 1e). Notably, these values surpass the CAR reported recently under similar experimental conditions[24], highlighting the strong performance of rBN as a photon-pair source. These observations confirm that the photon pairs originate from the SPDC process rather than from thermal bunching or substrate emission[15]. To further explore the dependence of SPDC efficiency on crystal thickness, we measured SPDC in three additional r-BN samples of varying thicknesses: 825 nm, 571 nm, and 463 nm (Supplementary Fig. 3). The results show SPDC coincidence rates of 2 Hz/mW, 1.6 Hz/mW, and 0.48 Hz/mW, respectively. Interestingly, the SPDC count rate does not scale linearly with crystal thickness, a behavior attributed to constructive and destructive interference effects within the crystal layers.

Polarization analysis of emitted photon pairs from r-BN flake

As h-BN, r-BN also has the hexagonal in-plane structure (Fig. 2a). The nonlinear polarization in this structure can be expressed by the equation $P_\alpha^{2\omega} = \varepsilon_0 \chi^{(2)}_{\alpha\beta\gamma} E^\omega_\beta E^\omega_\gamma$ where ε_0 is the vacuum permittivity, $\chi^{(2)}_{\alpha\beta\gamma}$ is the second order susceptibility and α, β, $\gamma = x$ or y, representing the in-plane directions in Cartesian coordinates. For a monolayer of BN, the nonvanishing tensor components of $\chi^{(2)}_{\alpha\beta\gamma}$ are: $\chi^{(2)}_{yyy} = -\chi^{(2)}_{yxx} = -\chi^{(2)}_{xxy} = -\chi^{(2)}_{xyx} = |\chi^{(2)}|$, with x and y corresponding to the zigzag and armchair directions, respectively[31,39]. In response, the whole nonlinear tensor will be symmetric when rotated over 60° periods. In our measurements, these directions are designated as H (horizontal) and V (vertical), respectively.

Initially, we align the polarization of both collection arms parallel to the pump field and rotate them simultaneously by rotating the HWP before the objective. As a function of the rotating polarization angle, the SPDC response of r-BN follows six-fold symmetry (Fig. 2b), consistent with the pattern in SHG experiment. This indicates that photon pair generation is maximized when the pump field aligns with the armchair direction and minimized along the zigzag direction, corresponding to the non-zero $\chi^{(2)}_{yyy}$ term. Furthermore, we set one collection arm's polarization perpendicular to the pump field while maintaining the other arm's parallel orientation. This configuration also displays a six-fold symmetry but shifts by 30 degrees compared to the initial co-polarized configuration (Fig. 2c). This indicates a high rate of photon pair generation when the pump field aligns with the zigzag direction, as expected from the nonzero $\chi^{(2)}_{xyx}$ term, where x-polarized light generates photons polarized in both x and y directions simultaneously.

Next, we fix the polarizations of the collection arms at a specific angle and rotate only the polarization of the pump field, resulting in a two-lobed symmetry pattern (Figure 2d-f). This can be well explained by considering that with a certain pump angle φ_P, the expected state will be $\Phi = \frac{\cos(\varphi_P)}{\sqrt{2}}(|HV\rangle + |VH\rangle) + \frac{\sin(\varphi_P)}{\sqrt{2}}(|HH\rangle - |VV\rangle)$. When the analyzers are

https://doi.org/10.1038/s41467-025-56436-2

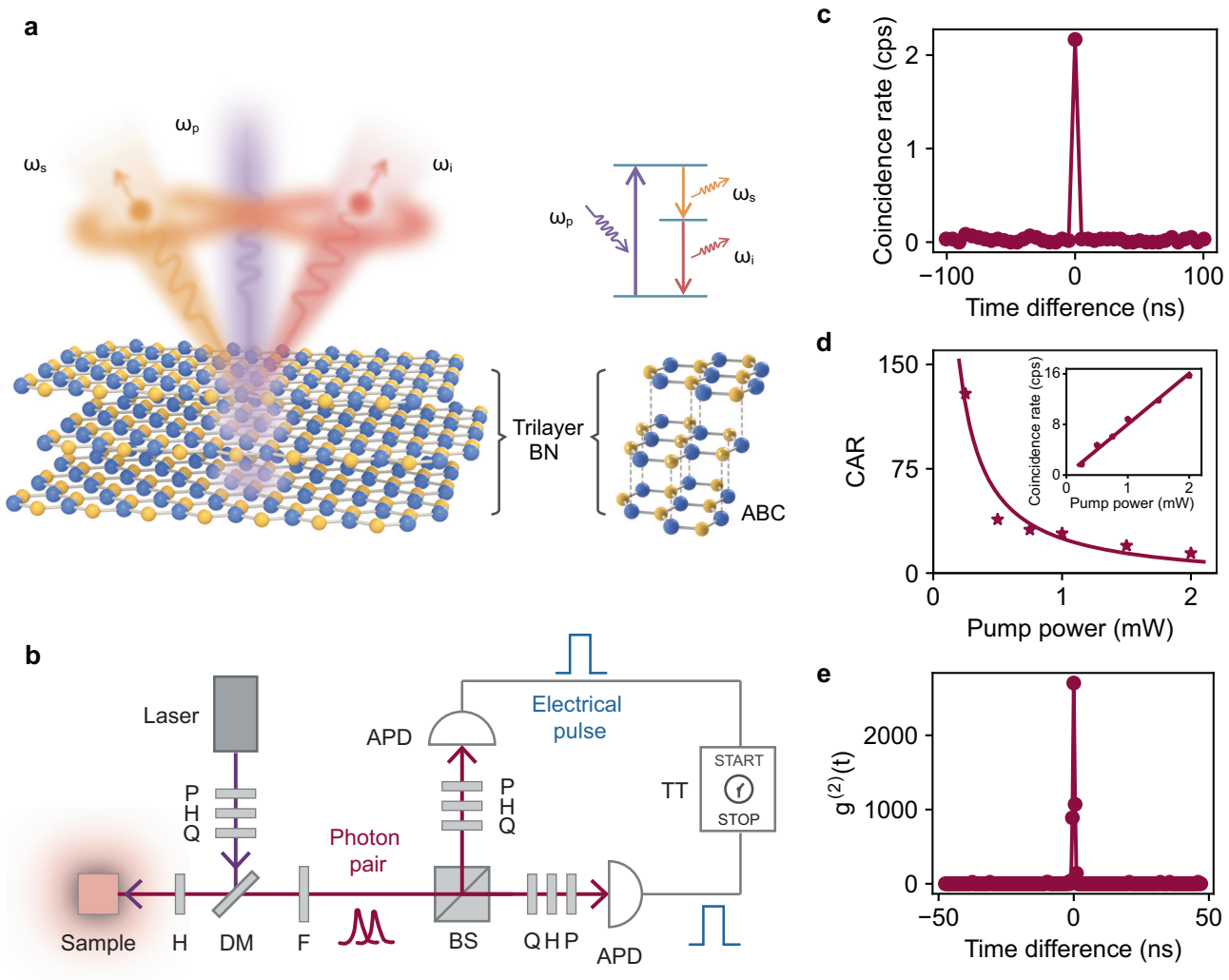

Fig. 1 | The experimental scheme for generating quantum entangled photons from a van der Waals insulator. a Schematic illustration of entangled-state generation in layered rhombohedral boron nitride (r-BN). A pump photon with frequency ω_p generates a pair of photons: a signal photon with frequency ω_s and an idler photon with frequency ω_i. **b** Setup used for characterization involving a 409 nm continuous-wave (CW) laser as the light source. Includes quarter-wave plate (Q), half-wave plate (H), and a polarizer (P) in the pump and collection arms to select desired polarization states. The signal in collection arms is filtered by a 750-long pass filter (F), coupled into a single-mode fiber and collected by avalanche photon diodes (APD). The electrical signals from APDs are analyzed by a time tagger (TT). DM, dichroic mirror. BS, beam splitter. **c** Coincidence measurement in r-BN in one minute. The coincidence count rate notably surpasses 2 Hz. The power of pump field is 0.25 mW. The bin width is set to 5 ns. **d** Coincidence-to-accidental ratio (CAR) in r-BN as a function of pump power, which exhibits an inverse relationship. The solid line represents the fitted curve. Inset: coincidence measurement in r-BN as a function of pump power, exhibiting a linear relationship. **e** Second-order correlation measurement in r-BN at a pump power of 2.5 mW, using a 12 nm bandpass filter. The bin width is set to 0.5 ns.

set at angle θ, the new measurement basis is transformed into the corresponding state at θ and $\theta + 90°$, which we define as $|+\rangle = \cos(\theta)|H\rangle - \sin(\theta)|V\rangle$ and $|-\rangle = \sin(\theta)|H\rangle + \cos(\theta)|V\rangle$, respectively. By setting both collection arms at the same angle, which results in the $|{+}{+}\rangle$ state, the coincidence rate is proportional to $\sin^2(\varphi_P + 2\theta)$ (Supplementary Note 3), which explains the observations in figures d-f. When the angles of both analyzers are set to 0, the coincidence rate follows $\sin^2(\varphi_P)$, peaking when the pump field aligns with the armchair direction (Fig. 2d). Additionally, as the analyzers are rotated by equal angles, the symmetry angle correspondingly shifts by double (Fig. 2e, f).

Verification of entanglement of photon pairs in r-BN

We next examined the entanglement of SPDC emission from the r-BN flake. By fixing the polarization of the pump field along the zigzag direction, equivalent HV and VH states are observed (Fig. 3a). This matches well the equal values of $\chi^{(2)}_{yxx}$ and $\chi^{(2)}_{xyx}$. Under these conditions, the generation of the Bell state $|\Psi^+\rangle = \frac{1}{\sqrt{2}}(|HV\rangle + |VH\rangle)$ is anticipated. To further verify the entanglement and symmetry properties of the generated state, we conducted the experiment in both diagonal-antidiagonal (D-A) and right-left circular (R-L) bases.

We project the H and V polarized states into D and A polarizations by adjusting the angles of polarizers and quarter-wave plates with the coincidence counts recorded thereafter. In this measurement setting, coincidence counts were maximized in the $|DD\rangle$ and $|AA\rangle$ configurations (Fig. 3b), expected for the Bell state $|\Psi^+\rangle$. Similarly, for the RL polarization measurements, QWPs were adjusted to specifically project the HV polarizations into R and L polarizations. When projected to the right-left circular basis, the $|HV\rangle + |VH\rangle$ Bell state translates to $|RR\rangle - |LL\rangle$, as shown in Fig. 3c.

By tuning the polarization of pump field to align with the armchair direction, a coherent superposition of $|HH\rangle$ and $|VV\rangle$ state is expected to be generated through $\chi^{(2)}_{yyy} = -\chi^{(2)}_{xxy}$ (Fig. 3d), corresponding to a different Bell state $|\Phi^-\rangle = \frac{1}{\sqrt{2}}(|HH\rangle - |VV\rangle)$. In the DA basis, the state translates to $|DA\rangle + |AD\rangle$, reflecting a shift from symmetric to antisymmetric configurations between diagonal and antidiagonal polarizations (Fig. 3e). Similarly, when measured in the RL

https://doi.org/10.1038/s41467-025-56436-2

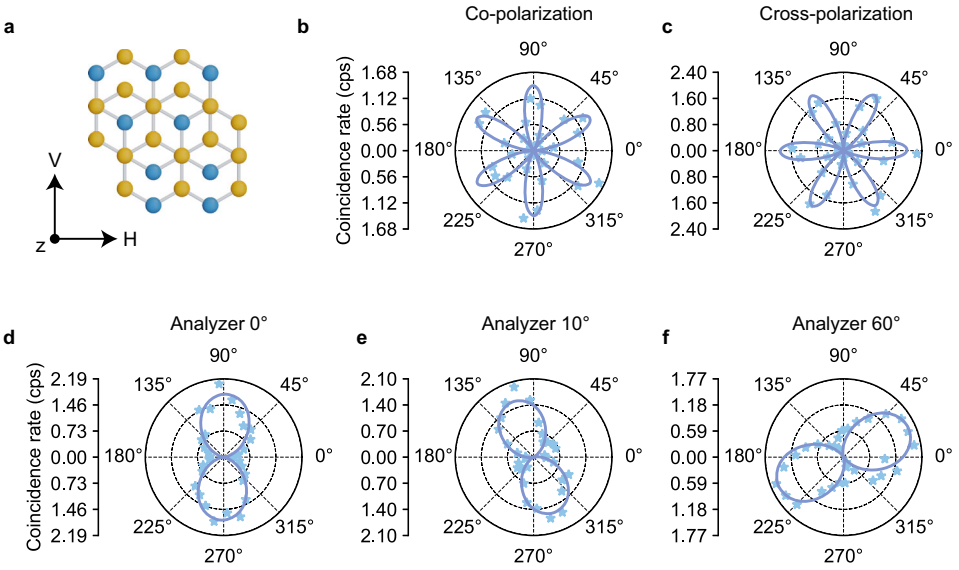

Fig. 2 | The polarization analysis for quantum entangled photons from a van der Waals insulator. a Illustration of crystal structure of r-BN. H is along the zigzag direction and V is along armchair direction of the crystal. **b** Coincidence count rate as a function of polarization of pump field in co-polarization configuration, where co-polarization denotes that the polarizations of both collection arms are set to parallel to the pump field. **c** Coincidence count rate as a function of polarization of pump field in cross-polarization configuration, where cross-polarization denotes that the polarization of one collection arm is set parallel and the other arm perpendicular to the pump field. **d**–**f** Coincidence count rate as a function of polarization of the pump field, with the angles of both analyzers fixed at 0°, 10°, 60° relative to the armchair direction. Star symbols represent experimental results, and solid lines indicate the fitted curves.

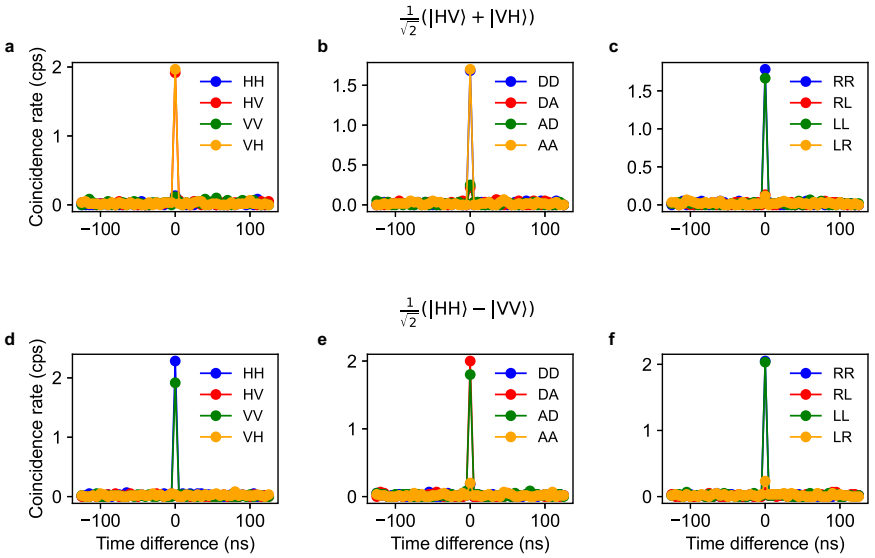

Fig. 3 | Coincidence measurements from r-BN in different measurement bases. **a**, **b**, **c** Coincidence counts measured from the r-BN when the pump field aligns with the zigzag direction, with measurement basis are along the **a** horizontal-vertical (H-V), **b** diagonal-antidiagonal (D-A), and **c** right-left (R-L) basis. These results indicate the Bell state $\frac{1}{\sqrt{2}}(|HV\rangle + |VH\rangle)$. **d**, **e**, **f** Coincidence counts measured from the r-BN when pump field aligns with the armchair direction, with measurement basis are along the (**d**) horizontal-vertical (H-V), **e** diagonal-antidiagonal (D-A), and **f** right-left (R-L) basis. These results indicate the Bell state $\frac{1}{\sqrt{2}}(|HH\rangle - |VV\rangle)$.

basis, the photon pairs state exhibits parallel alignment, yielding high counts for $|LL\rangle$ and $|RR\rangle$ (Fig. 3f). These findings affirm the entanglement of the generated photon pairs in r-BN and demonstrate the ability to realize switching between different Bell states by altering the pump field polarization in this van der Waals insulator, a capability that is not present in traditional quantum entanglement configurations.

Characterization of generated Bell state with quantum tomography

To fully reconstruct the density matrix of generated states from r-BN, we employed quantum tomography with 16 measurement settings[40]. First, we verified the $|\Phi^-\rangle$ Bell state by aligning the pump field along with the armchair direction of the crystal structure (Fig. 4a, b), and the reconstructed density matrix exhibited fidelity of 94.2 ± 3.8%, confirming the high quality of the generated quantum state. The degree of entanglement can be given by the concurrence C, which ranges from 0 (non-entanglement) to 1 (maximal entanglement)[41]. For the quantum state generated with the pump field aligned in the armchair direction, we got a concurrence value of $C = 0.932 \pm 0.033$. This value corroborates our other assessments, demonstrating significant entanglement. Furthermore, the purity of this state reached 95.6 ± 6.5%, indicating minimal mixed-state characteristics.

https://doi.org/10.1038/s41467-025-56436-2

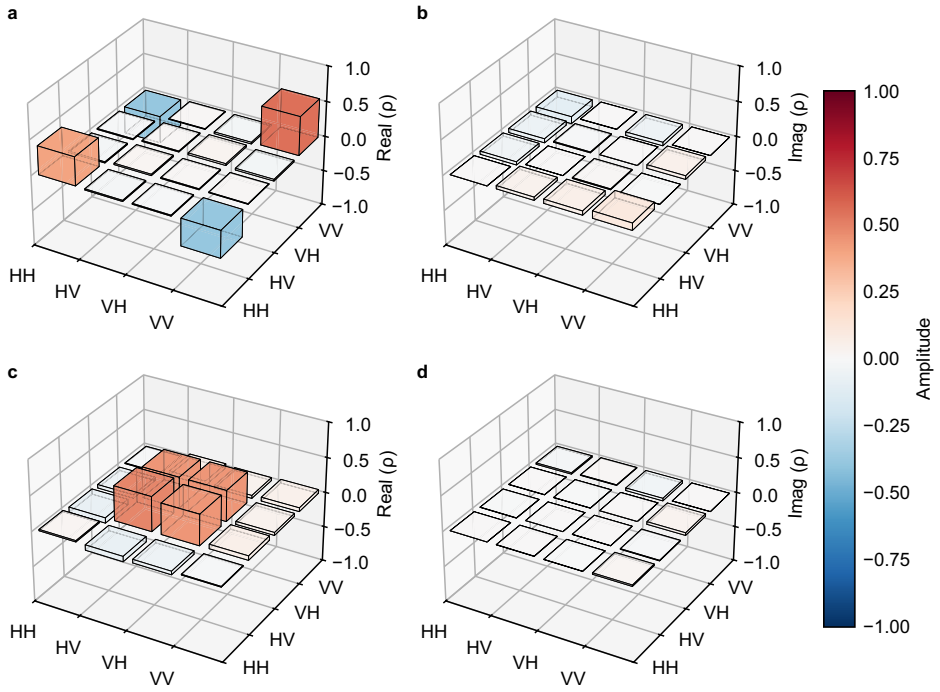

Fig. 4 | Quantum tomography of states generated from r-BN. Real (**a**) and Imaginary (**b**) part of density matrix of generated state from r-BN when pump field is along armchair direction of the crystal structure. Real (**c**) and Imaginary (**d**) part of density matrix of generated state from r-BN when pump field is along zigzag direction of the crystal structure.

In a parallel set of experiments with the pump field aligned along the zigzag direction of the crystal structure, the fidelity of the reconstructed density matrix is shown to be 92.4 ± 3.3%, corresponding to the $|\Psi^+\rangle$ state. The concurrence value of C = 0.916 ± 0.054 and a state purity of 88.2 ± 5.5% still reflect a high-quality quantum state, with slight variations from the armchair alignment. To confirm that the generated state is a Bell state, we placed an 850 nm long-pass filter in one arm and an 800 nm short-pass filter in the other arm to separate the signal and idler photons. The results of 16-state quantum tomography confirm that the generated state is indeed the Bell state $|HV\rangle+|VH\rangle$, with a fidelity of 95.0 ± 2.0% (Supplementary Note 4). These results highlight the high state quality from the entangled photon pairs generated from r-BN and illustrate the tunability of the quantum state generation in r-BN. Additionally, the entanglement fidelity measurements, summarized in Supplementary Table 1, confirm that fidelity remains above 90% across all tested pump powers, regardless of the pump polarization direction (zigzag or armchair). It further establishes r-BN as a robust platform for quantum entangled photon generation, capable of maintaining high fidelity as pump power varies.

Discussions

Our investigation into r-BN as a platform for entangled photon pair generation has unveiled promising advancements toward scalable quantum photonic devices. It highlights the potential of r-BN, a van der Waals insulator with wide optical band gap and broken out-of-plane symmetry, for the generation of entangled photons with high efficiency. The observed photon pair generation rate notably exceeds that of conventional 2D materials, underscoring r-BN's potential in quantum optical applications.

The structural distinction of r-BN, characterized by its ABC stacking, diverges notably from its hexagonal counterpart, presenting a pivotal enhancement in light-matter interaction essential for SPDC processes. By breaking the out-of-plane symmetry, r-BN facilitates the efficient conversion of pump photons into entangled photon pairs without the phase-matching constraints typically encountered in bulk nonlinear optical materials. Moreover, maintaining robust in-plane symmetry shows the capability to tune the Bell state generation by simply adjusting the pump polarization, which is a notable stride towards practical quantum technologies[42]. This tunability not only simplifies the operational complexity but also enhances the flexibility and applicability of r-BN-based devices in integrated quantum circuits.

Previous works have demonstrated the removal of phase matching conditions by utilizing ultrathin quantum emitters. These works, however, focus on more traditional materials with low nonlinear coefficients, and exhibit the need for precise angular alignment to access the nonlinear tensor components, further complicating their implementation in on-chip systems. More recently, polarization entanglement has been demonstrated in van der Waals materials, such as 3R-MoS_2[25], 3R-WS_2[24], and twisted $NbOCl_2$[28,29]. However, these studies either involve materials with significant photoluminescence that restrict operation to specific wavelength ranges or require complex device fabrication, such as multilayer twisting which hinders scalability and integration. Our work pushes the boundaries of these capabilities by introducing a flat-optics device based on r-BN, a van der Waals insulator with a wide optical bandgap that enables broad-spectrum transparency and operation across various pump wavelength ranges (down to 409 nm in our work). It further amplifies its suitability as a cleaner medium for quantum communication applications, where signal clarity and low background noise is paramount. Furthermore, our device eliminates the need for complex angular alignments or multilayer stacking, while offering dynamic control of quantum states.

Most notably, the real measured count rate, normalized to pump power and interaction length is 8667 Hz/(mW·mm) in our device, which is among the highest reported for thin-film sources (Supplementary Note 5). This performance, combined with the fabrication freedom of van der Waals materials and their seamless integration into on chip photonics, establishes our device as a versatile and scalable platform for quantum photonic devices.

Looking forward, the integration of r-BN into nanophotonic devices represents a significant opportunity for the development of more compact, efficient quantum optical systems. The layering capabilities offered by van der Waals forces could allow for novel designs of quantum circuits that incorporate multiple quantum states or interactions on a single chip, a feat that remains challenging with bulk materials[43,44]. Additionally, leveraging these properties in hybrid structures could potentially enhance the photon generation rates[45,46], pushing the operational boundaries of current quantum photonic technologies.

In conclusion, our findings not only pave the way for the use of r-BN in advanced quantum information science applications but also set a precedent for the exploration of other van der Waals materials in quantum technologies. The implications of these advancements extend beyond fundamental science into the realms of practical and scalable quantum technologies, marking a significant milestone in the quest for miniaturized and efficient quantum devices.

Methods

Sample preparation

The single-crystal FeNi foil (100 μm thick, 60 wt% Fe, Zhongke Crystal Materials Co. Ltd) was pressed onto the BN paper (90 μm thick, Guangdong Suqun New Material Co. Ltd) on a sapphire substrate and loaded into the tube furnace (Hefei Kejing Co. Ltd). The system was heated to 1250 °C for 3 h and maintained for 5 h at atmospheric pressure under the mixed flux (300 sccm Ar and 50 sccm H_2; sccm means standard cubic centimeter per minute). Then another gas flow of 300 sccm N_2 was introduced into the system to grow the r-BN thick layers. After growing for 60 h, the furnace is naturally cooled down to room temperature. In this process, the single-crystal FeNi substrate with the vicinal (111) surface was the key to achieve ABC stacking of r-BN. Firstly, due to the high solubility of B and N in FeNi alloys, the (B,N) atoms from the BN paper could continuously dissolve into the oneside surface, diffuse through the whole metal and precipitate at the opposite surface of the FeNi foil to form the BN thick layers. Then, the presence of atomic steps on the FeNi vicinal (111) surface guided the BN grains to be unidirectionally precipitated and seamlessly stitched into a single-crystal monolayer. Finally, the subsequent BN layers were precipitated with the same grain orientation as the first layer under the same growth condition and stacked in parallel to obtain the ABC stacking configuration. The r-BN films were directly peeled from the surface of r-BN/FeNi samples using the Scotch tape method and transferred onto the SiO_2/Si substrate.

Optical measurements

All our photon coincidence measurements utilized a home-built Hanbury Brown-Twiss setup, as depicted in Fig. 1b of the main text. Briefly, we employ a 409 nm continuous-wave (CW) laser to excite our sample within a back-reflection geometry. The laser beam is directed and focused onto the sample via a dichroic mirror (DM) and a microscope objective (50×, 0.8 NA). The back-reflected SPDC signal is transmitted back through the same objective and mirror. Photon pairs are split into two paths using a beam splitter. In each output path, a combination of a quarter-wave plate, a half-wave plate, and a polarizer is positioned, enabling the detection of arbitrary polarization states. The signals are then collimated into a single-mode fiber before being directed to avalanche photodiodes. The outputs from the detectors are processed by a time tagger (Swabian instruments) to perform coincidence detection. A long-pass filter with a cutoff at 750 nm is placed before the beam splitter to block any residual pump beam leakage and control the spectral range of the detected photon pairs. This setup allows for the detection of photons within the wavelength range 750–886 nm, whose effective bandwidth is 136 nm.

In our polarization-dependent experiments, we explore different configurations to observe the effects on photon pair generation. For the co-polarization setup shown in Fig. 2b, the polarizations of both collection arms are aligned parallel to the pump field. Varying polarizations are achieved by rotating the half-wave plate located before the objective, which simultaneously adjusts the polarizations of both the pump and the collection arms. For the cross-polarization configuration depicted in Fig. 2c, the polarization of one collection arm is set parallel and the other perpendicular to the pump field. Similar to the co-polarization setup, the half-wave plate before the objective is rotated to adjust both polarizations simultaneously. In the experiments where we aimed to fix the angles of analyzers, as illustrated in Fig. 2d–f, the polarizations of both collection arms are also adjusted simultaneously while half-wave plate before the objective is rotated, ensuring that the polarization of the collection arms remains consistent as intended throughout the experiment.

For full characterization of the state, we perform 16-measurement quantum tomography for the photon pairs obtained from pumping our sample. We chose a standard set of measurements according to what was convenient to take using our experimental setup. The input power for the measurements was 0.25 mW. For processing the quantum measurements, we used a maximum-likelihood method to construct the density matrix. The purity of the quantum state was calculated using the standard definition from quantum information theory, Purity=tr(ρ^2), where ρ is the density matrix of the quantum state and tr denotes the trace operation. We employed the general concurrence formula, which is an entanglement monotone, as follows:

$$\widetilde{\rho} = (\sigma_y \otimes \sigma_y)\rho^*(\sigma_y \otimes \sigma_y) \tag{1}$$

where σ_y is Pauli spin matrix and ρ^* is the conjugate of ρ.

$$R = \sqrt{\sqrt{\rho}\widetilde{\rho}\sqrt{\rho}} \tag{2}$$

and then we can get the eigenvalues of R, which are λ_1, λ_2, λ_3, λ_4, arranged in decreasing order. And the concurrence is defined as:

$$\mathcal{C}(\rho) = \max(\lambda_1 - \lambda_2 - \lambda_3 - \lambda_4, 0) \tag{3}$$

Data availability

Relevant data supporting the key findings of this study are available within the article and the Supplementary Information file. All raw data generated during the current study are available from the corresponding authors upon request.

References

1. Gisin, N. & Thew, R. Quantum communication. *Nat. Photonics* **1**, 165–171 (2007).
2. Valencia, A., Scarcelli, G. & Shih, Y. Distant clock synchronization using entangled photon pairs. *Appl. Phys. Lett.* **85**, 2655–2657 (2004).
3. Adachi, Y., Yamamoto, T., Koashi, M. & Imoto, N. Simple and efficient quantum key distribution with parametric down-conversion. *Phys. Rev. Lett.* **99**, 180503 (2007).
4. Shih, Y. Quantum imaging. *IEEE J. Sel. Top. Quantum Electron.* **13**, 1016–1030 (2007).
5. Lemos, G. B. et al. Quantum imaging with undetected photons. *Nature* **512**, 409–412 (2014).
6. Brida, G., Genovese, M. & Ruo Berchera, I. Experimental realization of sub-shot-noise quantum imaging. *Nat. Photonics* **4**, 227–230 (2010).
7. Zhong, H.-S. et al. 12-photon entanglement and scalable scattershot boson sampling with optimal entangled-photon pairs from parametric down-conversion. *Phys. Rev. Lett.* **121**, 250505 (2018).
8. Kwiat, P. G. et al. New high-intensity source of polarization-entangled photon pairs. *Phys. Rev. Lett.* **75**, 4337–4341 (1995).

9. Kwiat, P. G., Waks, E., White, A. G., Appelbaum, I. & Eberhard, P. H. Ultrabright source of polarization-entangled photons. *Phys. Rev. A* **60**, R773–R776 (1999).
10. Tanzilli, S. et al. Highly efficient photon-pair source using periodically poled lithium niobate waveguide. *Electron. Lett.* **37**, 26–28 (2001).
11. Tanzilli, S. et al. PPLN waveguide for quantum communication. *Eur. Phys. J. D. At. Mol. Optical Plasma Phys.* **18**, 155–160 (2002).
12. Santiago-Cruz, T. et al. Photon pairs from resonant metasurfaces. *Nano Lett.* **21**, 4423–4429 (2021).
13. Zhang, J. et al. Spatially entangled photon pairs from lithium niobate nonlocal metasurfaces. *Sci. Adv.* **8**, eabq4240 (2022).
14. Okoth, C., Cavanna, A., Santiago-Cruz, T. & Chekhova, M. V. Microscale generation of entangled photons without momentum conservation. *Phys. Rev. Lett.* **123**, 263602 (2019).
15. Santiago-Cruz, T., Sultanov, V., Zhang, H., Krivitsky, L. A. & Chekhova, M. V. Entangled photons from subwavelength nonlinear films. *Opt. Lett.* **46**, 653–656 (2021).
16. Sultanov, V., Santiago-Cruz, T. & Chekhova, M. V. Flat-optics generation of broadband photon pairs with tunable polarization entanglement. *Opt. Lett.* **47**, 3872–3875 (2022).
17. Sultanov, V. et al. Tunable entangled photon-pair generation in a liquid crystal. *Nature* **631**, 294–299 (2024).
18. Jia, W. et al. Polarization-entangled photon pair generation from an epsilon-near-zero metasurface. Preprint at https://doi.org/10.48550/arXiv.2405.03493 (2024).
19. Liu, Y., Huang, Y. & Duan, X. Van der Waals integration before and beyond two-dimensional materials. *Nature* **567**, 323–333 (2019).
20. Guo, Q. et al. Ultrathin quantum light source with van der Waals $NbOCl_2$ crystal. *Nature* **613**, 53–59 (2023).
21. Hong, H. et al. Giant enhancement of optical nonlinearity in two-dimensional materials by multiphoton-excitation resonance energy transfer from quantum dots. *Nat. Photonics* **15**, 510–515 (2021).
22. Li, Y. et al. Probing symmetry properties of few-layer MoS_2 and h-BN by optical second-harmonic generation. *Nano Lett.* **13**, 3329–3333 (2013).
23. Dogadov, O., Trovatello, C., Yao, B., Soavi, G. & Cerullo, G. Parametric nonlinear optics with layered materials and related heterostructures. *Laser Photonics Rev.* **16**, 2100726 (2022).
24. Feng, J. et al. Polarization-entangled photon-pair source with van der Waals 3R-WS2 crystal. *eLight* **4**, 16 (2024).
25. Weissflog, M. A. et al. A tunable transition metal dichalcogenide entangled photon-pair source. *Nat. Commun.* **15**, 7600 (2024).
26. Splendiani, A. et al. Emerging photoluminescence in monolayer MoS2. *Nano Lett.* **10**, 1271–1275 (2010).
27. Ma, J. et al. Polarization engineering of entangled photons from a lithium niobate nonlinear metasurface. *Nano Lett.* **23**, 8091–8098 (2023).
28. Kallioniemi, L. et al. Van der Waals engineering for quantum-entangled photon generation. *Nat. Photonics* 1–7 (2024).
29. Guo, Q. et al. Polarization entanglement enabled by orthogonally stacked van der Waals $NbOCl_2$ crystals. *Nat. Commun.* **15**, 10461 (2024).
30. Wang, L. et al. Bevel-edge epitaxy of ferroelectric rhombohedral boron nitride single crystal. *Nature* **629**, 74–79 (2024).
31. Qi, J. et al. Stacking-controlled growth of rBN crystalline films with high nonlinear optical conversion efficiency up to 1%. *Adv. Mater.* **36**, 2303122 (2024).
32. Hong, H. et al. Twist phase matching in two-dimensional materials. *Phys. Rev. Lett.* **131**, 233801 (2023).
33. Kuppadakkath, A. et al. Direct growth of monolayer MoS_2 on nanostructured silicon waveguides. *Nanophotonics* **11**, 4397–4408 (2022).
34. Löchner, F. J. F. et al. Hybrid dielectric metasurfaces for enhancing second-harmonic generation in chemical vapor deposition grown MoS2 monolayers. *ACS Photonics* **8**, 218–227 (2021).
35. Chen, H. et al. Enhanced second-harmonic generation from two-dimensional MoSe2 on a silicon waveguide. *Light.: Sci. Appl.* **6**, e17060–e17060 (2017).
36. Santiago-Cruz, T. et al. Resonant metasurfaces for generating complex quantum states. *Science* **377**, 991–995 (2022).
37. Li, P. et al. Infrared hyperbolic metasurface based on nanostructured van der Waals materials. *Science* **359**, 892–896 (2018).
38. Brown, R. H. & Twiss, R. Q. Correlation between photons in two coherent beams of light. *Nature* **177**, 27–29 (1956).
39. Yao, K. et al. Enhanced tunable second harmonic generation from twistable interfaces and vertical superlattices in boron nitride homostructures. *Sci. Adv.* **7**, eabe8691 (2021).
40. James, D. F. V., Kwiat, P. G., Munro, W. J. & White, A. G. Measurement of qubits. *Phys. Rev. A* **64**, 052312 (2001).
41. Wootters, W. K. Entanglement of formation of an arbitrary state of two qubits. *Phys. Rev. Lett.* **80**, 2245–2248 (1998).
42. Williams, B. P., Lukens, J. M., Peters, N. A., Qi, B. & Grice, W. P. Quantum secret sharing with polarization-entangled photon pairs. *Phys. Rev. A* **99**, 062311 (2019).
43. Giustina, M. et al. Significant-loophole-free test of Bell's theorem with entangled photons. *Phys. Rev. Lett.* **115**, 250401 (2015).
44. Ou, Z. Y. & Mandel, L. Violation of Bell's inequality and classical probability in a two-photon correlation experiment. *Phys. Rev. Lett.* **61**, 50–53 (1988).
45. Tang, Y. et al. Quasi-phase-matching enabled by van der Waals stacking. *Nat. Commun.* **15**, 9979 (2024).
46. Trovatello, C. et al. Quasi-phase-matched up-and down-conversion in periodically poled layered semiconductors. *Nat. Photon.* https://doi.org/10.1038/s41566-024-01602-z (2025).

Acknowledgements

This work is supported by Singapore Quantum engineering program (NRF2021-QEP2-01-P02, NRF2022-QEP2-02-P13), ASTAR (M21K2c0116, M24M8b0004), Singapore National Research Foundation (NRF-CRP22-2019-0004, NRF-CRP30-2023-0003 and NRF-MSG-2023-0002), Singapore Ministry of Education Tier 2 Grant (MOE-T2EP50221-0005, MOE-T2EP50222-0018), the National Natural Science Foundation of China (52025023).

Author contributions

Conceptualization, X.L., W.G., Methodology, X.L., L.K., R.Q., W.G., Material, H.H., K.L., Visualization, X.L., Y.Z., Supervision, J.P., W.G., K.L., Writing—original draft, X.L., W.G., Writing—review and editing, X.L., L.K., K.L., W.G.

Competing interests

The authors declare no competing interests.

Additional information

Supplementary information The online version contains supplementary material available at https://doi.org/10.1038/s41467-025-56436-2.

Correspondence and requests for materials should be addressed to Kaihui Liu or Weibo Gao.

Peer review information *Nature Communications* thanks the anonymous reviewers for their contribution to the peer review of this work. A peer review file is available.